Scientific and Technical Information

Edition CDR 5, pp. 17–34, 12/2001

Real space and Fourier microscopy of ordered suspensions

by T. Palberg and R. Biehl

Institut für Physik, Johannes Gutenberg-Universität, Mainz

Leica
MICROSYSTEMS

Real space and Fourier microscopy of ordered colloidal suspensions

by T. Palberg and R. Biehl

Institut für Physik, Johannes Gutenberg-Universität, Mainz

Abstract

Colloidal particles in aqueous suspension interact via long ranged screened electrostatic repulsion. Upon increasing the range and strength of the repulsion fluid, crystalline or glassy states are formed which in analogy to atomic substances are termed colloidal fluids, crystals and glasses. Despite structural equivalence significant differences exist. The softness of colloidal solids e.g. allows to access non-equilibrium shear stabilized structures. The Brownian dynamics on the other hand allow convenient access to solidification and other phase transition kinetics. Lattice constants are on the order of the wave length of visible light, while particle diameters range from a few nm to µm. Due to these specific length scales and the comparably slow diffusional dynamics colloidal suspensions are conveniently accessed via light scattering or microscopy. In this work we address two microscopic approaches realized on the same samples of ordering model latex spheres. One is the conventional high-resolution real space video microscopy. The other is a Fourier microscopy realized via introduction of a Bertrand lens into the imaging optics. In this case the equivalent of a two dimensional light scattering pattern is obtained. The combination of both techniques yields valuable information about both local and global, ensemble averaged properties of the sample.

Introduction

Colloidal crystals are fascinating objects first of all due to their optical properties. Fig 1 gives an example of nature's realization of colloidal crystal, an Australian natural gem opal of Cooper Peedy. Inside micron sized silica spheres are densely packed into regular arrays [1]. Such ordered structures may also be formed from synthetic particles and have become subject of intense research [1]. Typical examples comprise PMMA spheres in organic solvent [2, 3], charged Silica spheres [4] or, as in this work charged Polystyrene latex spheres [5, 6]. In the first case the phase transition is driven by entropy and results in face centred cubic packing (fcc) or for particle mixtures in densely packed alloy structures [2]. In the latter cases the particles repel each other via a screened Coulomb repulsion [7]. Instead of dense packing of hexagonal or cubic face centred order, the more open body centred cubic structure (bcc) results [5]. This was noted to be similar to the Wigner-crystallization of one-component plasma.

Fig. 1: Australian opal, a natural colloidal crystal

Reducing the particle concentration or particle charge, or adding some screening electrolyte the repulsion is weakened and the crystal melts. As attraction is still negligible a "supercritical" fluid results without phase separation into liquid and gaseous states [8]. Due to the softness of charged colloidal crystals, melting may also be obtained by applying shear to the sample, e.g. by simply shaking it [9]. In controlled experiments, e.g. in a plate-plate geometry or a capillary tube, different metastable structures are accessible for different shear rates [10] with hexagonal layers at low string phases and isotropic shear melts at large shear rates. After stopping shear, the shear melt starts solidification via nucleation and growth [11]. In slit cells, the combination of orienting shear and the presence of a flat wall acting as substrate, processes similar to melt epitaxial growth are observed. Large, nearly point-defect-free monolithic crystals result with the only defects given by twin domains [12, 13]. In very narrow slits further exotic structures were observed for nearly hard sphere repulsion [14]. Both kinds of objects are particularly interesting, as they may serve as novel materials for optical devices [15].

Due to the specific length scales colloidal suspensions may in principle conveniently accessed by simple yet powerful optical methods like light scattering and microscopy. Both yield valuable information on the sample structure in complementary ways. A very readable summary and prospect of methods, theoretical approaches and problems from condensed matter physics to be addressed was already given in 1984 [16]. Later on many of these suggestions experienced powerful and successful realizations and extensions [17].

In general, light scattering may be viewed as analogous to neutron or x-ray scattering. Albeit with a different contrast mechanism similar information on the particle structure, interparticle structure and particle dynamics may be obtained. From the discovery of visible Bragg reflections [18], most experiments on colloidal crystals so far were performed using a Debye-Scherrer like optical set-up resulting in powder averages of polycrystalline materials. For oriented single crystals also two-dimensional scattering patterns were recorded, e.g. to study annealing of stacking faults or the wetting of hard sphere crystals on a hard wall [19]. Apart from structure identification, average crystal sizes and for large particles with sufficiently slow dynamics also solidification kinetics may be inferred e.g. from the peak widths [20].

Microscopy on the other hand yields information on the local structure and sample morphology. Real space light microscopy is a very versatile tool, as for sufficiently large resolution and particle size it may directly reveal the spatial ordering [21] but on the other hand at lesser magnification shows the sample morphology [16]. In principle all conventional techniques may be employed like interference and phase contrast [13], confocal illumination [22] or polarization microscopy [23]. Interestingly, for sufficiently small numbers of individual crystallites in the light path, also crystals of cubic structure give rise to coloured patterns if observed between crossed polarizers. This is not due to optical anisotropy, but rather depends on the

change in polarization of the scattered light and is described by dynamic diffraction theory [24]. This was used in studies of the stacking fault structure of fcc crystals [25], new growth instabilities [23] or the reduction of nucleation rates under shear [26]. A particularly nice technique was employed by some authors, which relies on the combination of scattering and microscopy and was termed Bragg microscopy. Detailed studies on this technique with abundant examples for unusual and regular morphologies have been given by Okubo [27].

In this work we investigate charged sphere colloidal samples. They are conditioned at constant particle density and charge by adjusting the electrolyte concentration c using a recently described procedure. The sample is confined between the plates of a plate-plate shear cell of adjustable gap width. Disordered, fluid and bcc equilibrium structures can be prepared as well as non-equilibrium structures under shear. Structures are observed by two different microscopic methods: conventional high-resolution real space microscopy and Fourier microscopy. The latter will be shown to be equivalent to a two-dimensional light scattering experiment. We thus have access to two different and complementary informations from real and reciprocal space, respectively to local and ensemble averaged data. In the next section we shortly review some basic light scattering concepts. We then describe our instrument with the focus on the microscope optics and a short sketch of sample conditioning and sample cell. We demonstrate the performance of the instrument with samples of short range order in the following section. Finally we give some examples on crystalline equilibrium and non-equilibrium situations accessible and discuss the range of applicability of this instrument.

Experimental

We used Polystyrene spheres (PS301) of nominal diameter 2a = 301 nm [IDC, Portland, USA, Batch 10-66-58]. These we carefully characterized to obtain a static light scattering radius of a_{SLS} = (155.5 ± 1.2) nm [28]. The titratable number of surface charges was N = 2.3 x 10^4 and the effective charge from conductivity was Z* = 1980 [29, 30]. All sample conditioning follows procedures recently described in more detail. We only shortly note that the actual measuring cell is integrated into a closed tubing system. During conditioning the suspension is peristaltic pumped through a set of devices allowing precise adjustment and *in situ* control of the interaction parameters particle number density n and concentration of added electrolyte c. We further note that the concentration of residual impurities in general is negligibly small $c_B < 10^{-7}$ mol l^{-1} and that the contamination with airborne carbonate can be kept below 5 x 10^{-7} mol $l^{-1}h^{-1}$. At typical conditions of n ≈ 1 μm^{-3} and c = 5 x 10^{-6} mol l^{-1} residual uncertainties are on the order of 1% and 5%, respectively [29].

Two different optical pathways are realized in our instrument and sketched in Fig. 2a, b. In both cases samples were observed from below using an inverted microscope Leica DM IRB (Leica Wetzlar, D) mounted on a vibration-isolated table. The instrument provides sufficient space for mounting the optical shear cell. It allows for a flexible change of illumination from a tungsten halogen lamp to a λ_0 = 635 nm laser diode [ACM08/1630, Laser

Grafics, Klein Ostheim, D]. In both cases illumination is with parallel light. A central beam stop of 1.3 mm is usually applied to eliminate 0^{th} order diffracted (or non-diffracted) light from the detection path. Note that this is similar to dark field or ultramicroscopic illumination, where due to wide-angle illumination the 0^{th} order light passes outside the objective. Accordingly our images are constructed from diffracted light of order $O \geq 1$. Since the back focal plane of the objective is not directly accessible, the beam stop was adjusted directly in front of the objective lens.

In the Fourier mode an additional Bertrand lens is inserted in the light path. This leads to a real image of the back focal plane of the objective on the CCD-chip. The central beam stop covers angles of $\Theta \leq 15.1°$. The aperture of the objective collects light under angles $\Theta \leq 44.4°$. Thus the accessible range of scattering vectors is $3.5\ \mu m^{-1} \leq q \leq 7.2\ \mu m^{-1}$. For high-resolution real space observations we used a long distance, dry, 63x objective able to cover practically the whole range of plate-plate distances adjustable in the shear cell (maximum working distance ca. 1,800 µm) [PL Fluotar L 63x/0.7 corr PH2 ∞/0.1–1.3/C; Leitz Wetzlar]. The front focal plane (i.e. the objective in z-direction) can be adjusted over a range of 100 µm with an accuracy of 10 nm. This is achieved with a piezo electric drive [P 721.10, PI, Göttingen, D].

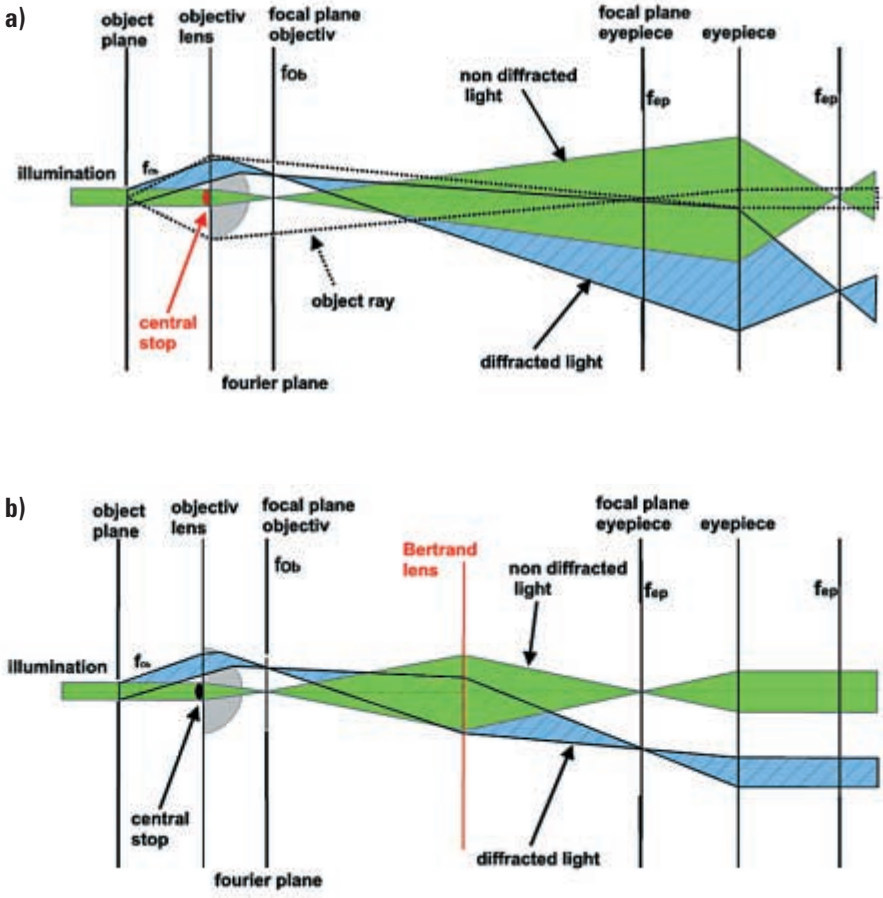

Fig. 2: Optical Pathway:
a) for real space micrography corresponding to dark field illumniation by inserting a central beam stop in front of the objective,
b) for Fourier microgprahy realized with an additional Bertrand lens between objective and eyepiece imaging the objective back focal plane onto the eyepiece focal plane.

We note that all optical components were chosen to be phase corrected. Resulting images are digitally recorded with a CCD-camera [CV-M10, Jai, Copenhagen, DK], and stored in a computer.

Several requirements had to be fulfilled in the construction of the plate-plate shear cell. The plate-plate distance should be variable to study influences of the cell walls on order formation and the shear rate should be variable over a large range to study a great variety of mechanical non-equilibrium conditions. To have reproducible shear conditions the cell was constructed to allow for adjustments of several degrees of freedom. It is mounted on a sturdy manual x-y-stage to choose the observation volume. A massive brass ring with PMMA fitting takes the lower quartz plate of 70 mm

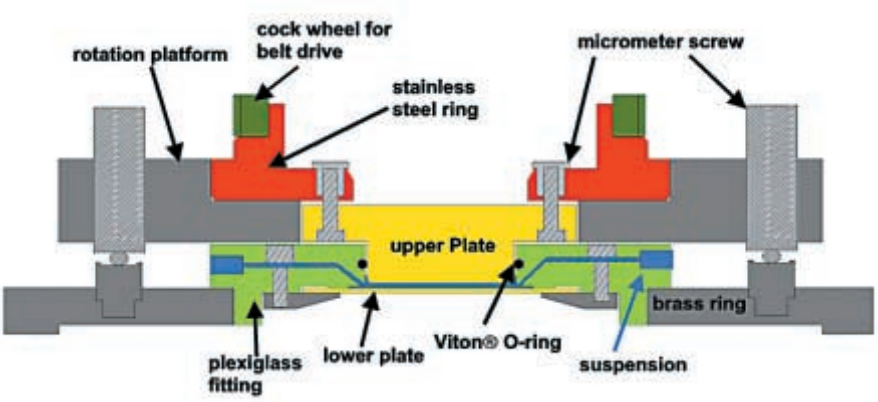

Fig. 3: Sketch of the plate-plate shear cell. The upper rotating plate is tumbled with 6 screws to adjust both plates parallel. The gap is filled through the connected tubing system for conditioning and sealed with a Viton® o-ring. The suspension volume is illuminated through the upper side and observed from below.

Fig. 4: Adjusted shear cell between illuminating condensor (top) and objective with central stop at the top (middle). Also visible the toothed belt drive on the cock-wheel and the micro-meter screws to adjust for planarity.

diameter and thickness 1 mm. The brass ring can be tumbled by a set of three micrometer screws to obtain the lower plate parallel to the x-y-stage and thus to the optical axis. On top of the brass ring the rotation platform for the upper plate is mounted. Here a stainless steel ring rotates in an outer brass part. The upper plate of height 18 mm and a lower diameter of 32 mm (top of the sheared volume) is fixed below this ring. Both quartz plates are polished to better than $\lambda/4$ planarity [Special edition, Hellma, Müllheim, D]. The lower plate can be adjusted by a second set of micrometer screws to obtain its lower surface perpendicular to the rotation axis. Its distance and co-planarity to the lower plate is independently adjusted by a third set of micrometer screws tumbling the whole upper part of the shear cell against the lower. In the experiments reported here the gap height was adjusted to 30 µm. A sketch of the instrument is shown in Fig. 3 and a view of the mounted cell in Fig. 4.

A cock-wheel is fixed on top of the stainless steel ring and rotated with a toothed belt drive. Rotation velocities can be varied from 0.025 to 0.5 RPM. At a plate separation of 30 µm and a radial distance of r = 10 mm off the centre this corresponds to shear rates of 0.25 Hz and 4.5 Hz, respectively. Shear rates were checked to be constant in time within 2 %.

The interaction parameters for sheared suspensions should be precisely adjusted and

Fig. 5: Bragg micrograph of a growing crystal at different times after cessation of shear. Up: 51 sec., down: 513 sec. The crystal (light grey) grows upward from the substrate (black) into the shear molten suspension (dark grey).

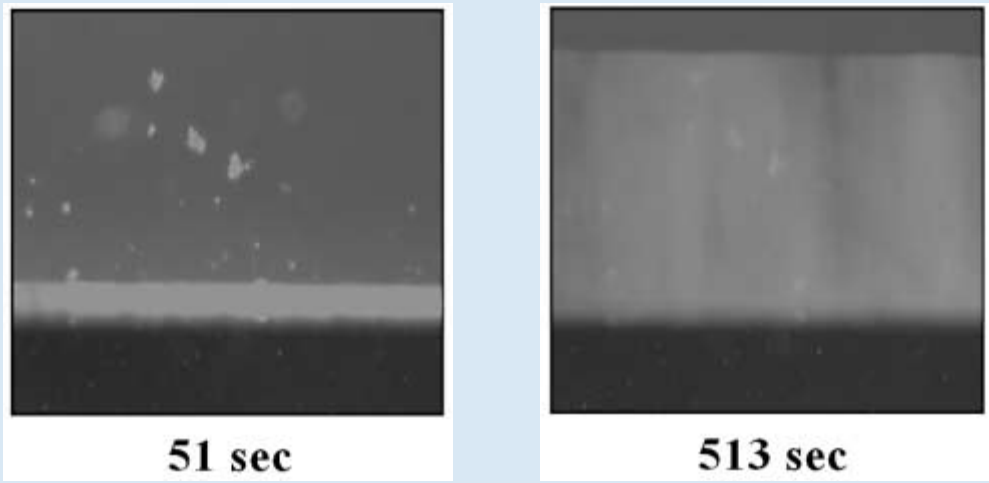

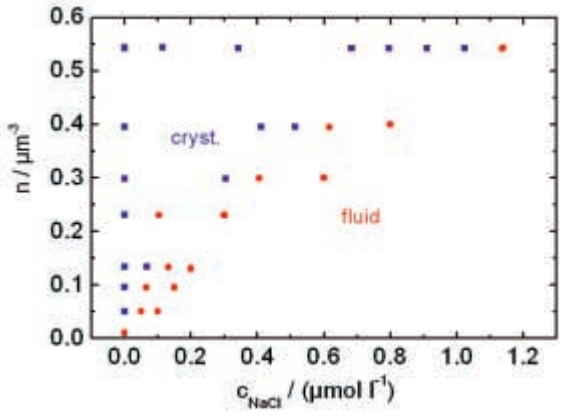

Fig. 6: Phase diagram of PS301. For the following examples the suspension was prepared in the lower part of the diagram at n = 5 x 10^{16}m^{-3} and n = 1 x 10^{17}m^{-3} for different salt concentrations.

kept stable inside the shear cell over several hours. To this end the PMMA fitting contains bores to rinse the cell with suspension and connect it to the preparation circuit. A delicate point is the sealing against air at the gap between lower and upper plate. Coverage with oil films or lamellae was observed to lead to incomplete sealing, respectively wearing of the lamellae. Good results were achieved with a free gliding Viton® o-ring sealing.

Instrumental performance

We first checked the suspension to display the expected structural behaviour. At mechanical equilibrium dilute, salty systems were found to stay in a disordered state. With increasing particle number density n and decreasing electrolyte concentration c a pronounced fluid order evolves. Further increase of interaction leads to the formation of colloidal crystals. Under deionized conditions (no added salt) the system shows a fluid-solid phase transition located approximately at n ≈ 0.08 µm^{-3}. With increasing salt concentration the phase boundary shifts to higher n-values and a coexistence region is observable. In the vicinity of the phase transition heterogeneous nucleation of wall based, twinned crystals dominates over homogeneous nucleation. A representative image of a crystal growing from the sidewall taken with Bragg-microscopy is given in Fig. 5. In Fig. 6 we present the lower portion of a phase diagram in terms of particle number density n and amount of added electrolyte NaCl. The equilibrium crystal structure of PS301 was in all cases observed to be bcc. This is in contrast to previous measurements on a smaller and slightly more polydisperse sample the scattering patterns of which are shown in Fig. 7 [31]. Note there the difference in the positions of the first order reflections. While for fcc an angle of 60° is observed between each reflection, the angle between top and side reflections is 71° for bcc. The PS301 phase diagram is, however, in accordance with the observations made on most other highly monodisperse systems. It further agrees well with model calculations based on a screened Coulomb pair interaction energy:

$$V(r) = (Z^{*2}e^2/4\pi\in)\,(\exp(\kappa a)/(1+\kappa a))^2\,\exp(-\kappa r)/r.$$

Z* is the effective charge, e the elementary charge, $\in=\varepsilon\varepsilon_0$ the dielectric constant of the medium, a the particle radius and r the interparticle distance. κ is the Debye screening parameter and its inverse, the screening length, is considered to constitute an estimate of

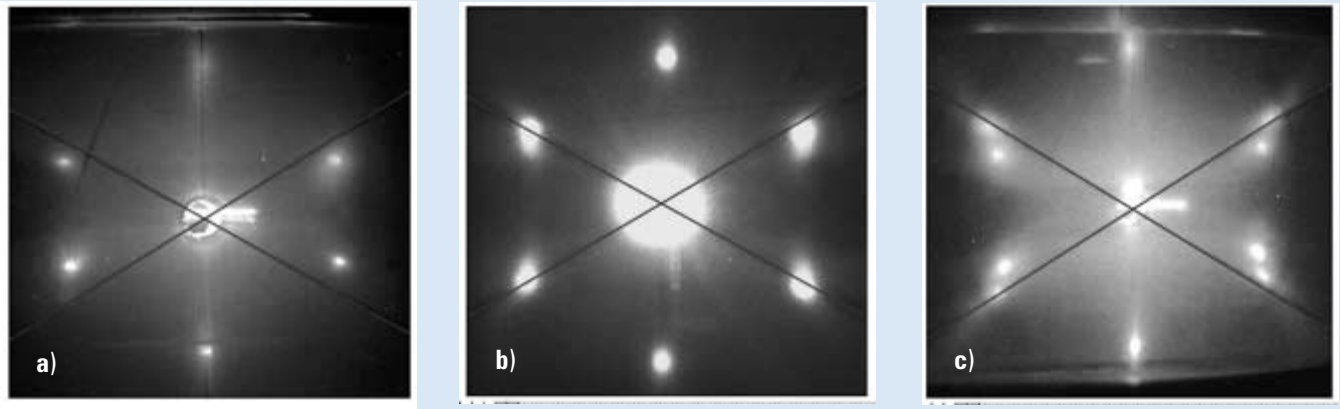

Fig. 7: Light scattering pattern for (**a**) bcc with two fold symmetric distribution of first order reflexes, (**b**) fcc with six fold symmetric distribution and (**c**) pattern for coexisting phases, also shown are lines as guide to the eye representing a 60° degrees symmetric pattern [31].

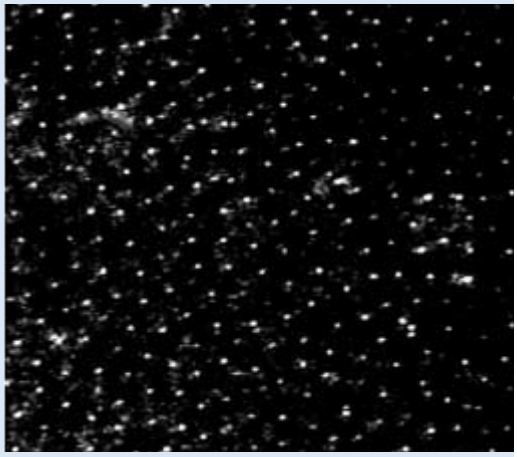

Fig. 8: Real-space micrograph (image width 60 µm) of PS301 particles at n = 5 x 10^{16}m^{-3} in the fluid phase.

the dimension of the double layer respectively the range of interaction. We thus judge our particles to display the expected phase behaviour and to be suited to perform a model study of well-defined structural properties.

We now turn to high-resolution images of the respective states of ordering. The real space micrograph of a suspension at a particle density of n = 5 x 10^{16} m^{-3} and at elevated salt concentration corresponding to a Debey-screening length of κ^{-1} < 50 nm is shown in Fig. 8. Only short range order is visible, i.e. there exists a correlation hole around each particle without any other particle inside and there further is a preferred average distance between particles of some 3 µm. Particles are not confined to layers, rather the micrograph shows all particles in a volume 50 x 50 µm^2 and of approximately 3 µm depth.

In Fig. 9 we show a layer off the cell wall of an oriented bcc crystal prepared at deionized conditions and n = 0.35 µm^{-3}. This corresponds to a volume fraction F = n 4/3 a_{SLS}^3 = 0.0048 and a bcc lattice constant of d_{100} = 1.8 µm. The image width of Fig. 9a is 100 µm. A single defect free crystal is visible which extended over an even larger area of some 200 x 900 µm and had the overall appearance of a cake slice. We note that this is due to the nucleation process after shear which for crystals wetting the wall will tend to produce a densely packed layer (110), for bcc; (111) for fcc parallel to the substrate and the densest packed direction <111> in the direction of formerly applied shear. A sketch of the bcc unit cell is given in Fig. 10. In our case of a plate-plate cell the direction of shear is concentric to the origin and several of these slices filled the whole sample cell distinguished by different orientations. Fig. 9b shows a magnified portion of Fig. 9a. The lines are guides to the eye indicating a portion of the imaged (110) plane. Note that further planes are visible in this image shifted by half a lattice constant. Particles positioned half way between the cube edges belong to layers above or below. At still higher packing fraction first a long-lived meta-stable state of registered hexagonal layers appears in which after some 10 to

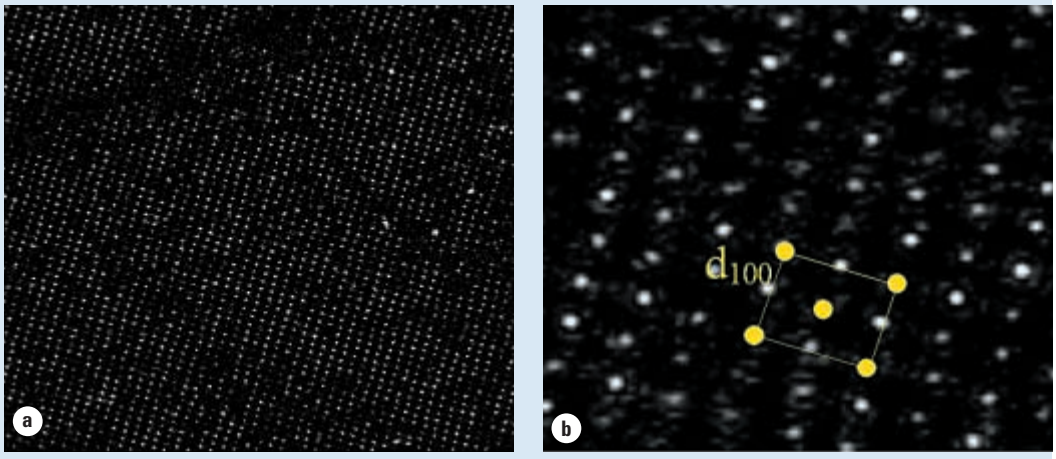

Fig. 9: (**a**) Real-space micrograph of PS301 (a) bcc crystal at n = 3.5 x 10^{17} m^{-3} (110) plane oriented parallel to the wall (image width 110 µm), (**b**) magnification of a portion of a, the sketch shows the (110) plane of the bcc unit cell d_{110} = 1.8 µm. Notice that also particles from the next plane are visible on the connection line.

Fig. 10 (left): Sketch of the bcc unit cell with the (110) plane hatched which is parallel top the wall. The arrow indicates the direction of formely applied shear (see Fig. 9).

Fig. 11 (right): Hexagonal layer matrix with a 4 x 5 bcc island (circled). Note that again a secon layer is visible.

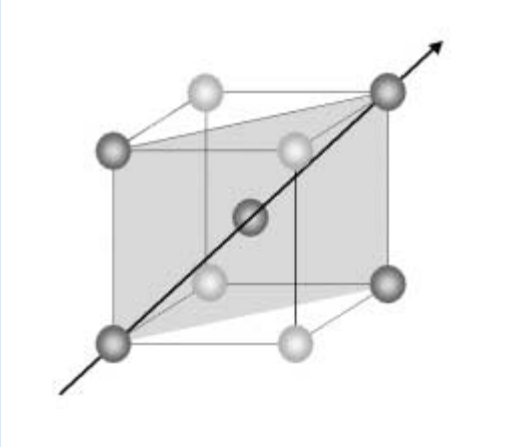

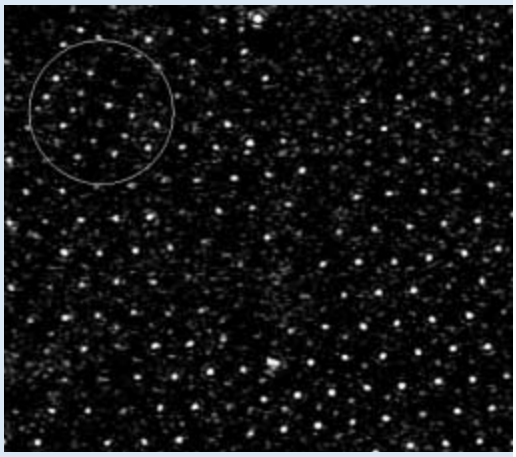

200 min islands of bcc structure nucleate. This is shown in Fig. 11 with the new island circled.

Under laser illumination with circularly polarized light we now inserted the Bertrand lens and observed the suspension again for different particle number densities and salt concentrations. In Fig. 12a we show the micrograph of a suspension of $n = 1 \times 10^{17} m^{-3}$ and c = 14 µmol l^{-1} salt added. This corresponds to a screening length much shorter than the interparticle distance of d_{NN} = 2.1 µm and even particle diameter 2a = 301 nm. No ordering is thus expected. The micrograph shows a nearly homogeneous radial intensity distribution with no azimuthal inhomogeneities. The central dark area is due to the beam stop and the outer black periphery due to the finite objective aperture. Also shown are the directions of scattering angle Θ and azimuthal angle φ. In Fig. 12b–e a series of four measurements are given recorded after stopping the pumping shear applied during conditioning. With decreasing salt concentration a ring-like pattern emerges. For Fig. 12c a second ring is faintly and for Fig. 12d clearly visible. At the lowest concentration a symmetric pattern of intensities is observed some 20 min after cessation of shear indicating the formation of crystalline order. If n is increased crystal formation proceeds much faster and the metastable layer phase of Fig. 11 shows a six-fold symmetric pattern as seen in Fig. 12e.

To interpret these micrographs we follow the general idea that they are equivalent to the two dimensional scattering patterns of Fig. 7. Then we have to consider a sample of particle number density $n = N/V_S$, where V_S is the scattering volume defined by the overlap of illuminating beam and detecting beam. The illuminating light is considered to be a linearly polarized plane wave: $\mathbf{E}(r) = \mathbf{E}_0 \exp(ik_i \bullet \mathbf{r})$, where the time dependence is omitted, as only elastic scattering is considered and $\mathbf{E}_0 = \mathbf{E}_0 \mathbf{n}_i$. The primary wave is incident on N spherical particles of radius a contained in V_S. Far from the sample the superimposed scattered fields may again be considered as a plane wave. The difference between incoming and scattered wave vector defines the scattering vector:

$$|\mathbf{q}| = |\mathbf{k}_i - \mathbf{k}_S| = (4\pi \nu_S/\lambda_0) \sin(\Theta/2)\,, \qquad (1)$$

where Θ is the scattering angle, ν_S is the solvent refractive index and λ_0 the vacuum wavelength of the (laser) light. For spherical particles $I(\mathbf{q})$ factorizes:

$$I(q) = C\, P(q) S(q) \qquad (2)$$

with the prefactor C:

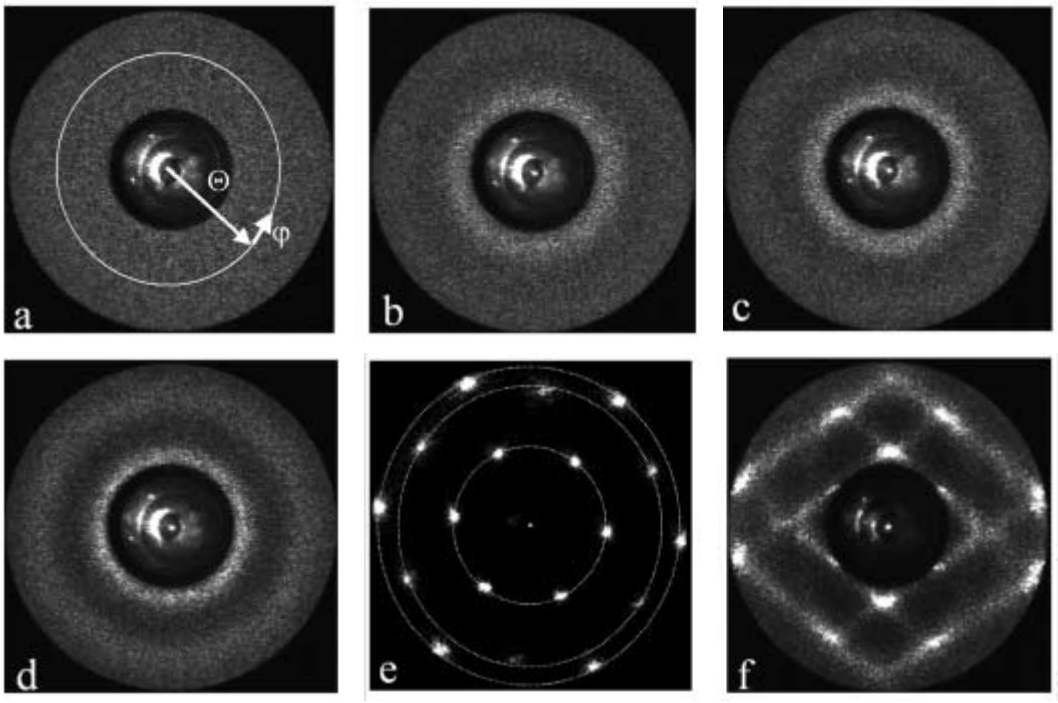

Fig. 12: Fourier micrographs at n = 1 x $10^{17}m^{-3}$ for different added salt concentrations c and screening lengths. Note that in the salt free case 0.1 µmol H^+ and OH^- from the self-dissociation of water and in additonal the counter ions dissociated from the particles contribute to the screening length κ^{-1}. (**a**) c = 14 µmol H_2CO_3, κ^{-1} = 80 nm gas like, scattering angles are also shown, (**b**) c = 0.52 µmol H^2CO^3, κ^{-1} = 350 nm, (**c**) c = 0.32 µmol H_2CO_3, κ^{-1} = 400 nm, (**d**) c = 0.07 µmol H_2CO_3, κ^{-1} = 540 nm, (**e**) no added salt, κ^{-1} = 610 nm, metastable phase directly after cessation of shear with six fold symmetry, (**f**) no added salt, κ^{-1} = 610 nm, 20 min after cessation of shear; considerable structural rearrangements have occured.

$$C = \frac{V_S I_0}{R_D^2} \frac{\mathbf{k}_i^4}{(4\pi)} \frac{N}{V_S} (\mathbf{n}_i \cdot \mathbf{n}_S)^2 b(0)^2 \qquad (3)$$

comprising the geometry of the scattering experiment and the optical properties of the particle material. Here $I_0 = {}^1\!/_2\,(\varepsilon_s/\mu_0)^{1/2}E_0^2$ is the incident intensity, R_D is the distance between V_S and the detector. $\mathbf{n}_0$ and $\mathbf{n}_S$ are the polarization vectors of incident and scattered light, respectively. In our set-up circularly polarized light is used to avoid asymmetric scattering patterns due to polarization.

We thus consider two mutually orthogonal, linearly polarized beams of phase lag $\lambda/2$. The arithmetic mean of both contributions to $(\mathbf{n}_i \cdot \mathbf{n}_S)^2$ then results in a factor $(1+\cos^2(\Theta))/2$ for the Θ-dependence of scattered intensity [32]. The particle scattering amplitude at zero wave vector is proportional to the particle volume times the difference in refractive indices of particles and solvent: $b(0) \propto (4/3)\pi a^3 (\nu_P - \nu_S)$. The particle form factor $P(q) = b(q)^2/b(0)^2$ is normalized by $b(0)^2$ to result in $P(0) = 1$. It describes the q-dependence of single particle scattering. In particular, for small Polystyrene spheres ($\nu_P = 1.590$) of a < 60 nm in water ($n_S = 1.333$) it often is sufficient to use the Rayleigh-Debye-Gans approximation for small q data:

$$P(q) = \left[3 \frac{\sin(qa) - qa\cos(qa)}{(qa)^3} \right]^2 \qquad (4)$$

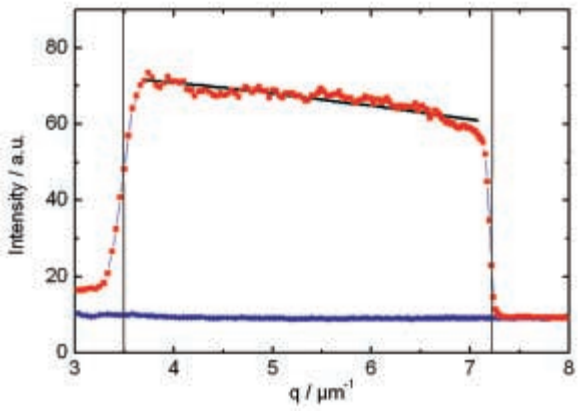

Fig. 13: φ-averaged intensity distribution of Fig. 12a (red squares), also shown is the measured background intensity from pure water nearly equal to the black level of the CCD camera (blue circles).
The additional red line corresponds to a RDG particle form factor combined with a $(1+\cos^2(\Theta))/2$ correction considering polarisation effects. The vertical lines represent the accessible q range limited by the central stop at low and the objective aperture at high q, respectively.

Polydispersity, bimodal mixtures, deviations from spherical shape and the corresponding influence of particle orientation may also be treated within extensions of this approximation [33]. For larger particles and those with radial variations in ν_P Mie scattering theory applies [34], for inelastic (dynamic) light scattering see e.g. [35].

Fig. 12a showed the Fourier micrograph of a diluted, salty suspension. At this low particle density and high concentration of added salt no structure formation is expected nor observed (S(q) = 1). We detect a slight but smooth radial decrease of scattered intensity. In Fig. 13 we performed an angular average over φ to obtain the scattered intensity as a function of q. Arbitrary units of the absolute grey scale of the video system are given. Scattering vectors q were calculated using the radial position of a pixel in relative units (i.e. 0 at the centre and 1 at $r_{aperture}$, the position of aperture):

$$q(w) = \frac{4 \cdot \pi \cdot \nu_S}{\lambda} \cdot \sin\left(\frac{1}{2} \cdot \arcsin\left(\frac{1}{\nu_S} \cdot \sin\left(\arctan\left(w \cdot \frac{r_{aperture}}{f_{objective}}\right)\right)\right)\right) \qquad (5)$$

Here $f_{objective}$ denotes the focal length of the objective and ν_w is the refractive index of water. The two vertical lines denote the theoretical limits of the accessible range of scattering vectors corresponding to the central stop and objective aperture, respectively. At large $q > 7.4\ \mu m^{-1}$ a dark count background of about 8–10 units is visible. The background at $3.5\ \mu m^{-1} < q$ is slightly larger due to parasitic stray light (Note that the inner beam stop is not completely black in Fig. 11) and the transition is less sharp as at the outer boundary. Both presumably is due to the position of the central stop, which is applied to the front lens of the objective instead of the Fourier plane. In addition, the blurring results from the gradual change of the size of V_S with Θ. I(q) shows some statistical scatter on the order of some 5–10 units which is due to the diffusive fluctuations of scatterer positions and not present in the dark count measurement performed on a sample of deionized, filtered water. Since it contains the information about the diffusive motion it could in principle used as input for a speckle correlografic experiment [36]. Averaging over several images could further enhance the statistical accuracy of the static measurement. Apart from this scatter the signal decreases monotonously over the accessible range of scattering vectors. We compare our data to a form factor *P*(*q*) calculated using Mie theory for monodisperse spheres of radius 155.5 nm, corrected for circular polarization and multiplied with a constant to meet the experimental data

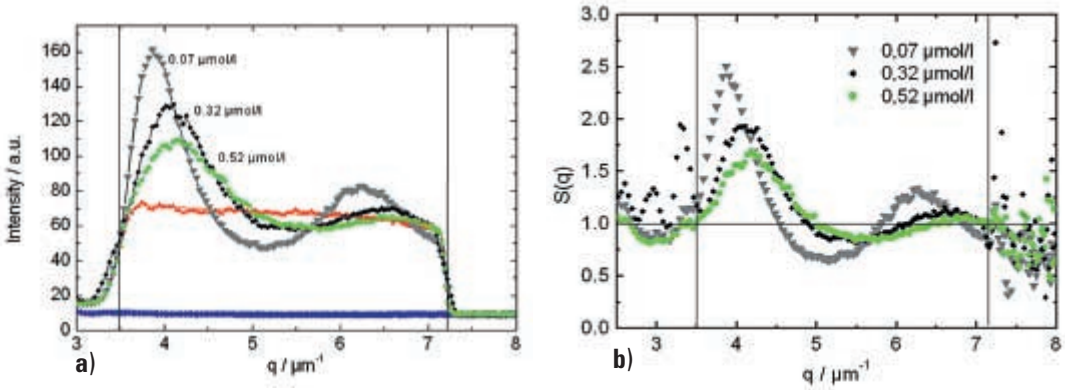

Fig. 14: (**a**) Averaged intensity distribution corresponding to Fig. 12a–12d. For increasing salt concentration the fluid like structure disappears, (**b**) background corrected intensities of Fig 12b–12d divided by the background corrected structure less intensities of Fig 12a for 3.5 $\mu m^{-1} < q < 7.2\ \mu m^{-1}$. This is interpreted as the structure factor of the fluid suspension.

at the q = 5 μm^{-1}. Considering the statistical accuracy of some 5% the agreement is very satisfying over the range of 3.7 $\mu m^{-1} < q < 7.2\ \mu m^{-1}$.

S(q) contains all the information about the particle positions $\mathbf{r}_i$. It equals unity for all scattering vectors if no interparticle ordering occurs. S(q) is defined as:

$$S(\mathbf{q}) \equiv \frac{1}{N} \sum_{i=1}^{N} \sum_{j=1}^{N} \left\langle \exp\left(i\mathbf{q} \cdot (\mathbf{r}_i - \mathbf{r}_j)\right) \right\rangle \tag{7}$$

where the brackets <...> denote the ensemble average. S(q) differs for differently structured phases. In the colloidal fluid particles possess short range order. The particle positions are usually represented by the radial distribution function g(r). The structure factor depends only on the modulus of **q** and is connected to g(r) through its Fourier transform:

$$S(q) = 1 + n \int_{V_s} d\mathbf{r}\, (g(r) - 1) \exp(i\mathbf{qr}) \tag{8}$$

g(r) shows a pronounced peak followed by decaying oscillations for increasing r. The main peak of S(q) thus represents the most prominent spatial frequency of g(r). In Fig. 14a the φ-averaged scattered intensities are shown for the suspensions of Fig. 12a–d, while Fig. 14b shows the static structure factors for the same data set. These were calculated dividing the background corrected φ-averaged intensities of the ordered samples by that of the disordered sample in Fig. 12a. Note the large scatter of data for $q < 3.5\ \mu m^{-1}$ and $q > 7.2\ \mu m^{-1}$ present in curves b and d. Curve c in addition shows some systematic deviation towards high values in the range just outside the actual measuring range. This is not fully understood, but disappears, if the micrographs are taken some ten minutes after stop of preparational pumping. As the relaxation into the equilibrium structure should occur on the time scale of milliseconds for these low concentrations, we rather suspect that the pumping pressure may lead to a minute shift of the plate distance relaxing on a longer time scale and thus to a slight distortion of the measured intensities. The magnitude of deviations from one outside the measurement range in both cases is due to the fact that S(q) results from the division of two small numbers.

As expected the intensity of the main peak increases with increasing interaction, while its position q_{MAX} shifts towards smaller q-values. If $q_{MAX} \approx 2\pi/d_{NN}$ is interpreted as a measure of mean interparticle distance d_{NN}, the particles stay further apart. This corresponds to an enhanced centering of particles, the growth of the correlation hole in g(r), and the emerging of a pronounced short range order.

For long ranged crystalline order the distribution of particles $\rho(\mathbf{r})$ is a periodic function. In reciprocal space this corresponds to a set of lattice vectors $\mathbf{g}_{hkl} = h\mathbf{b}_1 + k\mathbf{b}_2 + l\mathbf{b}_3$ forming the reciprocal lattice (where h, k, l are the Miller indices). From the squared modulus of the Fourier transform of $\rho(r)$ an ideal crystalline structure factor $SC(\mathbf{q})$ may be derived. For the infinite crystal this is a set of delta functions. For lattices with more than one lattice point per unit cell selection rules determine the h, k, l for which scattering is observed. For bcc the sum of miller indices has to be even, for fcc the indices have to be either all odd or all even. Intensity in the case of an ideal infinite crystal is observed, whenever $\mathbf{q} = \mathbf{g}_{hkl}$.

Following this argument the appearance of many Bragg-reflections in the Fourier-micrographs is somewhat surprising. However, finite crystal dimension may lead to a broadening of the individual Bragg spots in the corresponding direction of reciprocal space, in the limit of a two-dimensional array of spherical scatterers an arrangement of Bragg-rods results. In addition, also for an fcc lattice with stacking faults (111) and (311) are transformed to Bragg rods [19]. Thus for real crystals intensity is observed whenever the Ewald sphere intersects with $S(\mathbf{q}) \neq 0$. To illustrate this we refer to Fig. 12f giving the Fourier-micrograph of the registered hexagonal layer structure of Fig 11. Following Heymann et al. [19], Fig. 15 shows the reciprocal space in directions parallel and perpendicular to the incident beam for an oriented crystal of stacked hexagonal planes with the Ewald construction for our experiment. The reader is referred to [19] for a discussion of the basic but nevertheless tricky crystallography used in this construction. The hexagonal planes may be stacked either in ABABAB, ABCABCABC or in a more or less random sequence to result in hexagonal, cubic face centred or random stacked close packing, respectively. Fcc reflections usually appear as threefold symmetric pattern, a single stacking fault however is sufficient to generate six-fold symmetric pattern. The symmetry of the respective reflections is indicated via the symbols. The Ewald sphere has a radius of $a_C\nu_S/\lambda = 7.18$ and intersects with the random

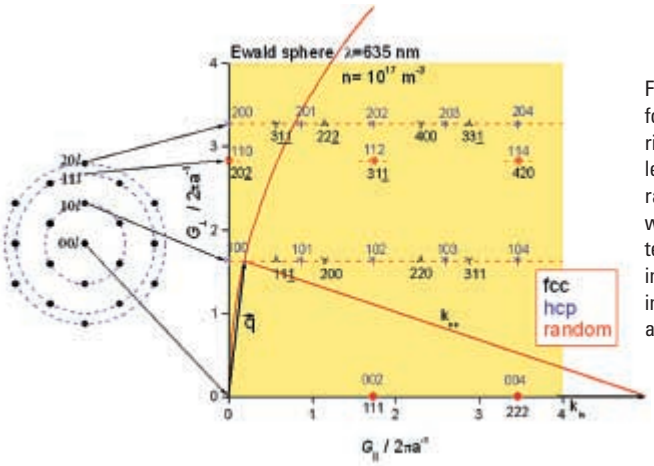

Fig. 15: Left: sketch of the k_x-k_y plane in the reciprocal space for a system of hexagonal layers at k_2=0 (G⊥ plane). On the right the G⊥ axis represents the radial component from the left for all φ and the G component corresponds to k_2. For random stacking we obtain along complete rods intensitieys whicch grow at the indicated point sif the overall structure tens to be more fcc (Y) like ore more hcp (*) like. The upper indices are in hexagonal notation for hcp and the lower are in cubic notation for fcc. Also given ist the Ewald sphere for a particle density n = 1 x 1017m^{-3} and λ = 635 nm.

stacking broadened (100) and (200) rod (hexagonal indexing). It is much further off the finite size broadened (20$\underline{2}$) reflection. Consequently the observed intensity distributions of Fig. 12f shows a low intensity for the second set of hexa-gonally arranged spots. We note that this distribution is due to the choice of λ and via the lattice constant subject to experimental conditions. Thus both for neutron scattering and for light scattering on hard spheres different intensity distributions may be observed [19, 37].

We close this section with two remarks on the experimental realization and the analysis procedure. First we note that the Fourier micrographs may also be taken under white light illumination. An example is given in Fig. 16a. Here the central beam stop was not applied to record the full-multi-coloured scattering pattern. The Bragg reflections appear radially stretched and show a rainbow-like pattern with blue situated at smaller radial positions. The image can be understood considering the definition of the scattering vector, which is different in magnitude for different wavelengths. Thus different scattering angles result. Scattering intensity is observed for all cases, however, as the reciprocal structure of real space layers is a set of Bragg rods.

The micrograph was taken of a rather concentrated suspension with a high shear rate of some 15 Hz applied. Note that two inner reflections are missing. Such pattern were observed before and explained using the appropriate Ewald construction for hexa-gonal layers sliding over each other, each in the grooves of the adjacent ones [37].

The second remark concerns an alternative evaluation procedure performing a numerical Fourier analysis of the real space micrographs. In this case the two-dimensional Fourier transform of the projection of the particle positions results. This does not contain the full three-dimensional position information but may nevertheless yield valuable first information about typical length scales and especially about orientational correlations. Many examples of this standard technique may be found in the literature [16]. We

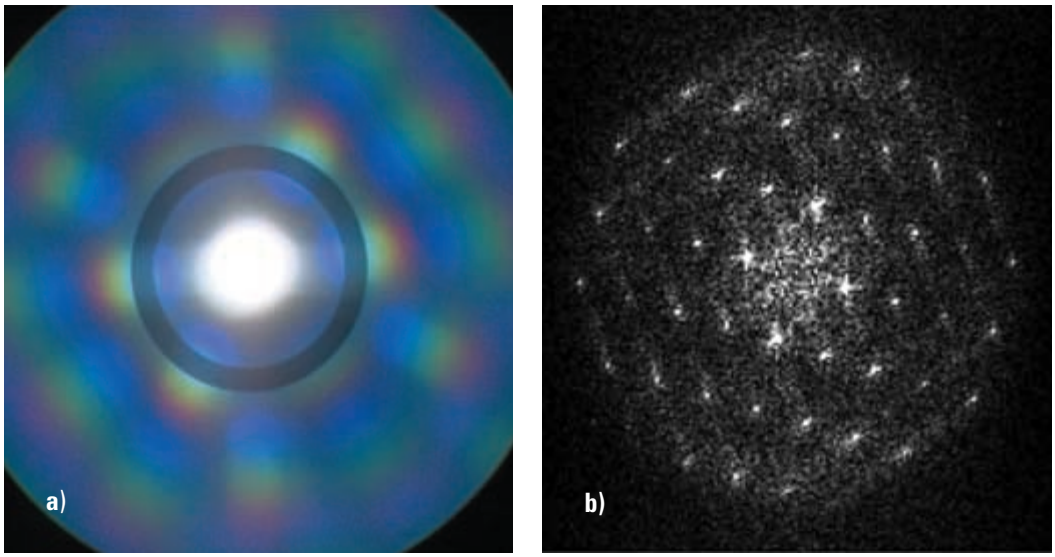

Fig. 16: (**a**) Scattering pattern under white light illumination, scattering patttern are the same as for laser illumination but with a rainbow like coloured band caused by different intersection point of rods in k-space and Ewald sphere changing radius with wavelength see also Fig. 15. (**b**) Numerical Fournier transform of Fig. 8 resulting in the image of a bcc crystal.

here only present one example in Fig. 16b, namely the numerical Fourier transform of Fig. 8 showing the image of a bcc crystal. A rectangular pattern results, which is rotated by 90° as compared to the original.

Discussion

In the last chapter we have shown that the patterns observed in the Fourier mode can be qualitatively understood in terms of two-dimensional scattering patterns from three-dimensional lattices. A quantitative evaluation following the procedures usually applied to conventional light scattering results should face no principle difficulties. E.g. fluid structure factors may be compared to Monte Carlo computer simulation results or to integral theoretical approaches using appropriate closure relations like the Percus-Yewick closure for hard or the Rogers-Young closure for charged spheres, respectively [33]. Apart from this our set-up may provide further information not accessible in pure scattering experiments. As first example we note that the small bcc crystallite visible in the real space micrograph of Fig. 11 is not visible as separate scattering pattern in the corresponding Fourier micrograph. This is perfectly understandable as the volume of the crystallite is very small as compared to that of the matrix phase. Further, close inspection of Fig. 11 shows not all particles to be perfectly in plane. Instead some appear less intense due to a slight in-layer corrugation present in the system. This corrugation is hardly seen for layers adjacent to the solid cell wall. There all particles appear equally bright. It rather evolves upon retreating from the solid substrate. Note that the corrugation wavelength is on the order of a few dozen particles. The amplitude is estimated from

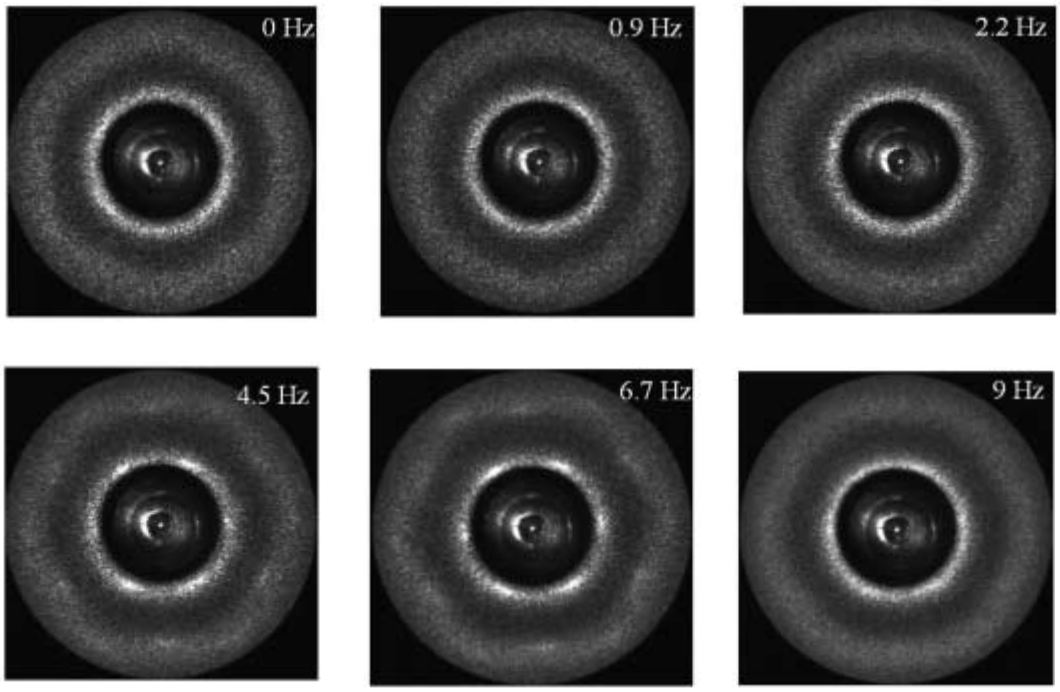

Fig. 17: Series of scattering patterns at n = 1 x $10^{17}m^{-3}$ and salt concentration of 0.1 µmol H_2CO_3 for different shear rates. The first and second maxima of a fluid structurre factor in mechanical equilibirum are visible. For low shear rate $\gamma < 2.2$ Hz there is no change, for 4.5 Hz and 6.7 Hz we dind an additional hexagonal pattern superimposed on both maxima indicating the evolution of a triangular odering driven by the applied shear. For a higher shear rate of 9 Hz this structure vanishes again.

focussing experiments to be on the order of a few tenths of the layer spacing. Similar excitations were also reported for few layer systems of incommensurate plate spacing where particles were observed to undergo jumps between well discriminated heights. In our case the amplitude seems to be a smooth function of lateral position. This rather reminds of the thermal excitation of standing shear waves as well known from bulk samples [31] but with different wavelength due to the different resonator geometry. In the Fourier pattern this corrugation is not to be discriminated from other kinds of particle displacement (like Brownian motion about the lattice site) and only contributes to the overall broadening of peaks and the background.

All above experiments were performed without applied shear. With the plate-plate shear cell we can also systematically subject the sample structure to two different shear experiments. Either the suspension is forced under hydrostatic pressure difference to flow between the two (stationary) plates or the upper plate is rotated with respect to the lower. The set-up further differs from other experiments, in that very narrow slit geometries may flexibly be realized. An example of a plate-plate shear experiment is given in Fig. 17 a–f. A series of Fourier micrographs were taken at different rotation frequencies. The local shear rate is determined from the plate distance (from interference measurements on a reflected laser beam) and the calibrated stepper motor speed. The experiment started from a suspension in the fluid regime prepared as close as possible to freezing. In the first micrograph a hexagonal pattern is very faintly visible, if one concentrates on the low intensity region between first and second fluid maximum. Under shear this symmetry first disappears, then reappears together with clearly discernible peaks positioned at the q_{MAX} of the fluid scattering pattern. At the largest shear rates these patterns disappear again. At no stage, however, the fluid scattering pattern is completely lost. This observation is somewhat counter-intuitive as shear is expected to destroy long-range order. On the other hand it is well known from investigations of concentrated suspensions that hexagonal layers may be formed or destroyed depending on the shear rate and this in fact was used to explain the shear thinning behaviour observed in rheological experiments [37, 38]. Also the coexistence of several different phases under shear flow through a capillary was reported [39]. What is really unexpected is the coexistence of two superimposed scattering patterns coexisting in a situation where the shear rate should be independent of vertical position. Two possible explanations are at hand. Either the layer phase tries to nucleate homogeneously inside the sheared fluid. In this case one may imagine that we observe fluctuations not reaching the critical dimension necessary for subsequent growth. On the other hand one could also suspect an influence of the cell wall in the sense that the non-equilibrium phase diagram is dependent on the plate spacing. In this case in addition a non-linear velocity profile or discontinuities in the shear rate would be expected to appear. Both alternatives are currently checked using time resolved real space imaging, but it is still too early to give a resolution for this interesting question.

Conclusion

The combination of real space and Fourier microscopy turned out to be a

valuable source of information on equilibrium phase behaviour, morphology, phase transition kinetics and structure development under non-equilibrium conditions. Since the suspensions investigated here are model systems for both atomic solids and fluids and on the other hand for industrially relevant dispersions the results gained using this method may gain considerable impact on the solution to fundamental condensed matter problems and technical application. In addition the interaction potential is sufficiently tractable to back our observations with computer simulations of various kinds and compare it to theoretical approaches. The technique on the other hand bears also a high didactic potential, since all basic concepts of scattering and real space imaging enter in a straightforward way. In fact it is used in our institute both on the undergraduate and graduate level to explain and illustrate scattering problems in condensed matter physics. Finally we remark that this paper dealt with the technical realisation more than with the investigated physics and that more work is under way to be published elsewhere.

Acknowledgements
Financial support of the Deutsche For-schungsgemeinschaft (SFB 262, Pa459/7-2,3) and the Materialwissenschafliches Forschungszentrum Mainz are gratefully acknowledged.

Bibliography

[1] **J. V. Sanders:** Nature 204, 1151 (1964); J. V. Sanders, M.J. Murray, Nature 275, 201 (1978)
[2] **P. Bartlett, W. van Megen,** in: A. Mehta, Granular Matter (Springer New York, 1994), 195–257.
[3] **S. E. Phan, W. B. Russel, Z. Cheng, J. Zhu, P. M. Chaikin, J. H. Dunsmuir, R. H. Ottewill:** Phys. Rev. E 54, 6633 (1996).
[4] **T. Okubo:** in K. S. Schmitz (ed.): Macro-ion characterization: from dilute solution to complex fluids, ACS Symposium Series 548, 364 (1994).
[5] **Y. Monovoukas, A. P. Gast:** J. Coll Interface Sci. 128, 533 (1989).
[6] **W. J. Hunt, C. F. Zukoski:** J. Colloid Interface Sci. 210, 332 (1999).
[7] **A. K. Arora** (ed.): Ordering and Phase Transitions in Colloidal Systems, VCH, New York 1995.
[8] **C. F. Tejero, A. Daanoun, H. N. W. Lekkerkerker, M. Baus:** Phys. Rev. E 51, 558 (1995).
[9] **B.J.Ackerson:** Physica A 128, 221 (1983).
[10] **T. Palberg, M. Würth:** J. Phys I (France 6; 237-244 (1996).
[11] **T. Palberg:** J. Phys. Condens. Matter 11: R323 (1999)
[12] **M. R. Maaroufi, A. Stipp, T. Palberg:** Prog. Colloid & Polym. Sci 108; 83 (1998).
[13] **M. S. Elliot, B. T. F. Bristol, W. C. K. Poon:** Physica A 235, 216 (1997).
[14] **S. Neser, C. Bechinger, P. Leiderer, T. Palberg:** Phys. Rev. Lett. 79, 2348 (1997).
[15] **J. C. Crocker, D. G. Grier:** MRS Bulletin 23, 24 (1998); C. Murray: ibid. 33 (1998); A. van Blaaderen: ibid. 39 (1998); S.A. Asher, J. Holtz, J. Weismann, G. Pan: ibid. 44 (1998).
[16] Proceedings of the "Atelier d´Hiver sur les Cristeaux colloideaux", Les Houches 1985, J. Phys. (France) C-3 46.
[17] **B.J. Ackerson** (ed.): Phase Transitions 21 (2–4), (1990).
[18] **W. Luck, M. Klier, H. Wesslau:** Ber. Bunsenges. Phys. Chem. 67, 75 (1963); ibid. 84.
[19] **A. Heymann, A. Stipp, Chr. Sinn, T. Palberg:** J. Colloid Interface Sci. 206 119 (1998).
[20] **J. L. Harland, W. van Megen:** Phys. Rev. E 55, 3054 (1996).
[21] **C. A. Murray, D. G. Grier:** Ann. Rev. Phys. Chem. 47, 421 (1996).
[22] **N. A. M. Verhaegh, J. S. van Duijneveldt, A. van Blaaderen, H. N. W. Lekkerkerker:** J. Chem. Phys. 102, 1416 (1995).
[23] **A. P. Gast, Y. Monovoukas:** Nature 351 553 (1991).
[24] **P. A. Rundquist, P. Photinos, S. Jagannathan, S. A. Asher:** J. Chem. Phys. 91, 4932 (1989).
[25] **Y. Monovoukas, A. P. Gast:** in B. J. Ackerson (ed.): Phase Transitions 21 (2–4), 183 (1990).

[26] **T. Palberg, W. Mönch, J. Schwarz, P. Leiderer:** J. Chem. Phys 102, 5082 (1995).
[27] **T. Okubo:** in K. S. Schmitz (ed.): Macro-ion characterization: from dilute solution to complex fluids, ACS Symposium Series 548, 364 (1994).
[28] **N. Garbow, J. Müller, K. Schätzel, T. Palberg:** Physica A 235, 291 (1997).
[29] **M. Evers, N. Garbow, D. Hessinger, T. Palberg:** Phys. Rev. E 57, 6774 (1998).
[30] **D. Hessinger, M. Evers, T. Palberg:** Phys. Rev. E (in Press 2000).
[31] **H.-J. Schöpe, Th. Decker, T. Palberg:** J. Chem. Phys. 109, 10068 (1998).
[32] **J. D. Jackson,** Classical Electrodynamics New York, Wiley & Son (1962) chapter 9.6.
[33] **G. Nägele:** Phys. Reports 272, 217 (1996).
[34] **H.C. van de Hulst:** Light scattering by small particles Dover, New York 1981.
[35] **J. K. G. Dhont:** An introduction to the dynamics of colloids, Elsevier, Amsterdam 1996.
[36] **E. Bartsch, V. Frenz, S. Kirsch, W. Schärtl, H. Sillescu:** Prog. Colloid Polym. Sci. 104, 40 (1997).
[37] **W. Loose, B. J. Ackerson:** J. Chem. Phys. 101, 7211 (1994).
[38] **H. M. Laun, R. Bung, S. Hess, W. Loose, O. Hess, K. Hahn, E. Hädicke, R. Hingmann, F. Schmidt and P. Lindner:** J. Rheol. 36, 1057 (1993).
[39] **T. Palberg, M. Würth:** J. Phys I (France) 6, 237 (1996).

Authors' address:
Dipl. Phys. Ralf Biehl, Prof. Dr. Thomas Palberg, Institut für Physik, Johannes Gutenberg-Universität Mainz, Staudinger Weg 7, D-55099 Mainz